Supporting Information

Muskan Jain[1, 2], Mayur Jagdishbhai Patel[3], Lingli Liu[4], Jeny Gosai[2,5], Manish Khemnani[1,2], Himangshu Gogoi[6], Mun Yin Chee[4], Antonio Guerrero[7], Wen Siang Lew[4], Ankur Solanki[1, 2,*]

[1]*Department of Physics, School of Energy Technology, Pandit Deendayal Energy University, Raysan, Gandhinagar 382426 India.*
[2]*Flextronics Lab, Pandit Deendayal Energy University, Gandhinagar, Gujarat 382426, India.*
[3]*Department of Chemistry, Indian Institute of Technology Guwahati, Guwahati 781039 Assam, India.*
[4]*School of Physical and Mathematical Sciences, Nanyang Technological University, Singapore, 637371*
[5]*Department of Chemistry, School of Energy Technology, Pandit Deendayal Energy University, Raysan, Gandhinagar 382426 India.*
[6]*Department of Electrical Engineering, Indian Institute of Technology Guwahati, 781039 Assam, India*

[7]*Institute of Advanced Materials (INAM), Universitat Jaume I, 12006 Castello, Spain*

*Corresponding Author: ankur.solanki@sot.pdpu.ac.in

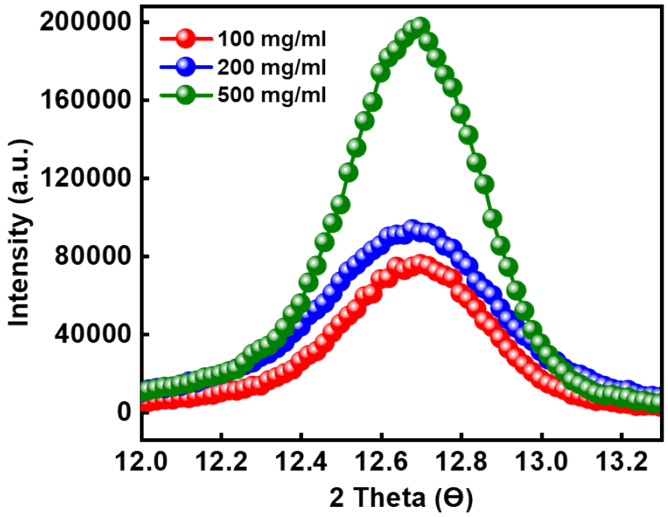

Figure S1: The enlarged view of XRD diffraction peak (001) of all three solution concentrations.

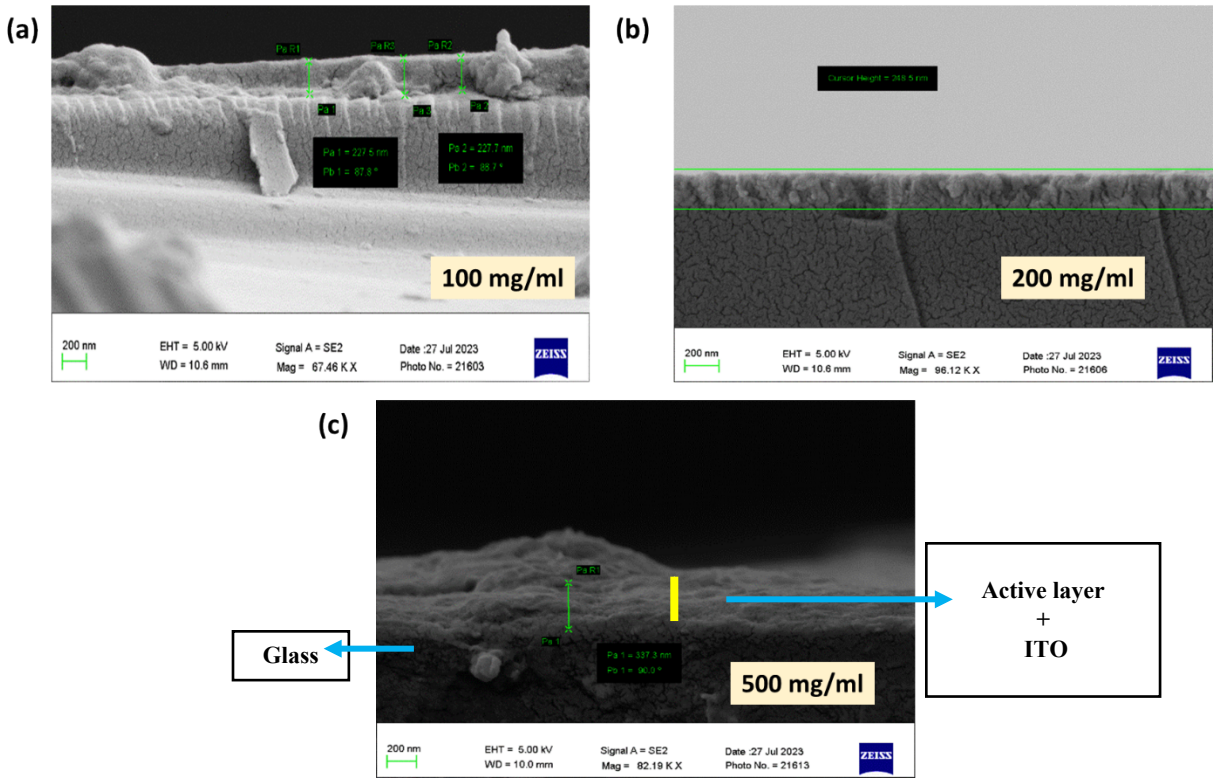

Figure S2: Cross-sectional SEM view for ITO/PbI_2 of three solution concentration used for the study (a) 100 mg/ml (b) 200 mg/ml (c) 500 mg/ml.

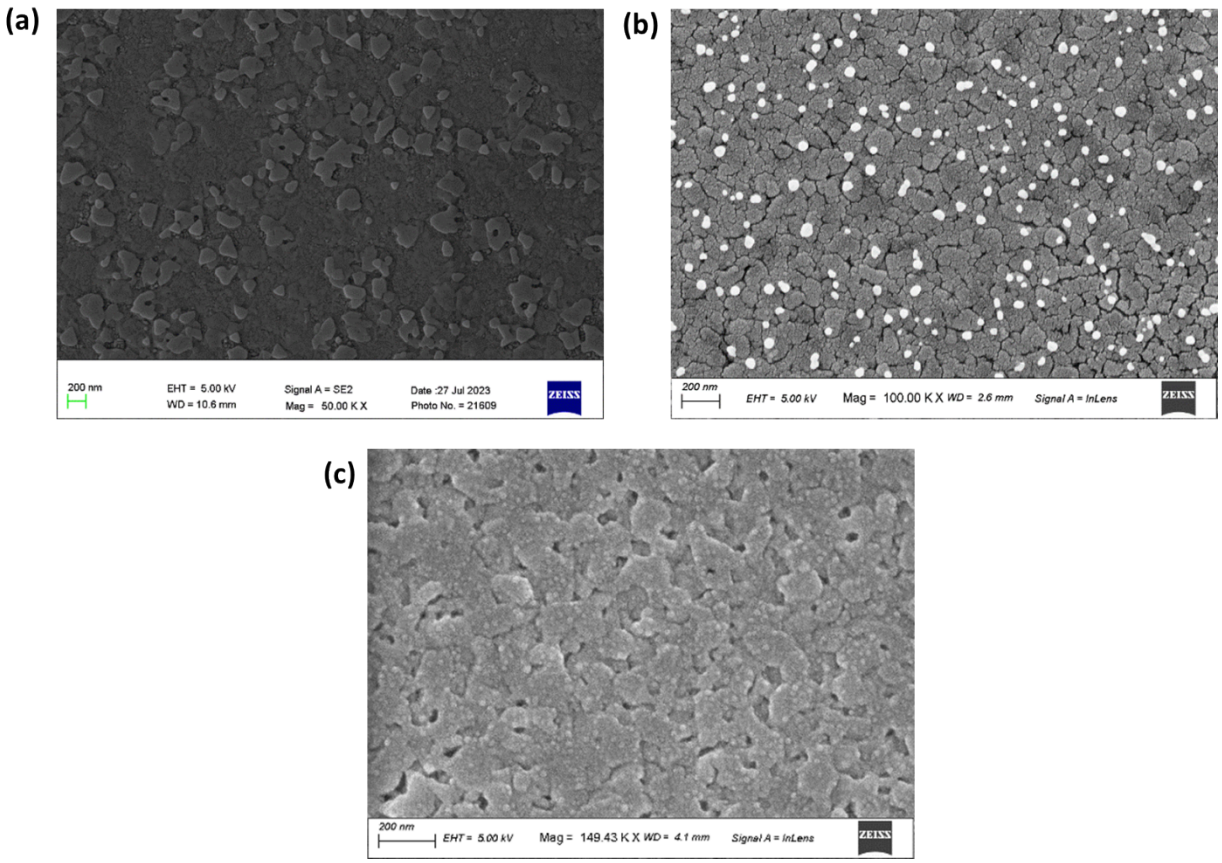

Figure S3: Top SEM view of PbI_2 thin films morphology of three solution concentration used for the study (a) 100 mg/ml (b) 200 mg/ml (c) 500 mg/ml.

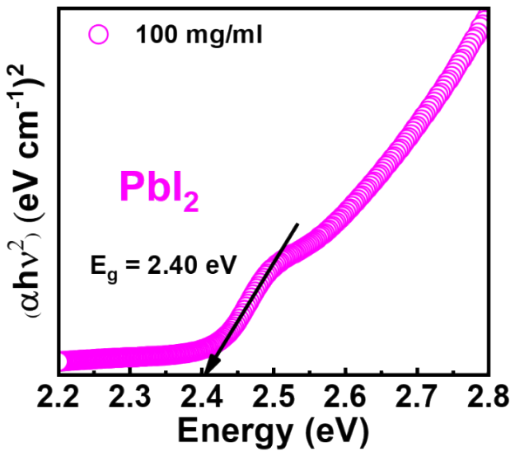

Figure S4: Tauc plot of UV- visible spectra of PbI_2 thin film of solution concentration 100 mg/ml.

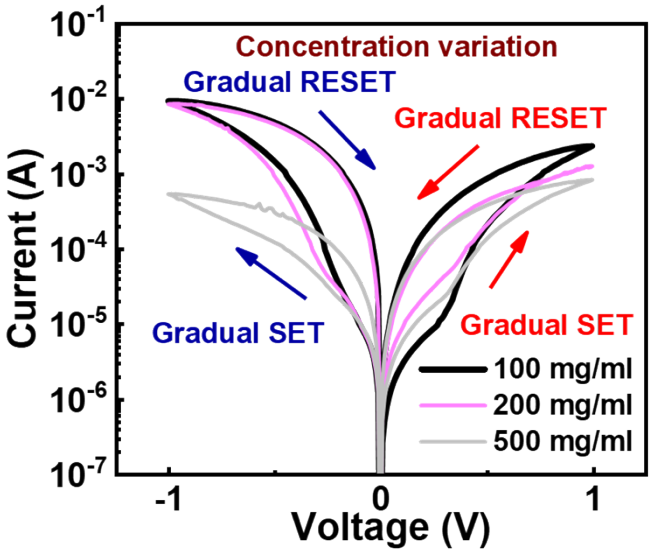

Figure S5: I-V characteristics of memristor device recorded for different solution concentrations (100, 200 and 500 mg/ml).

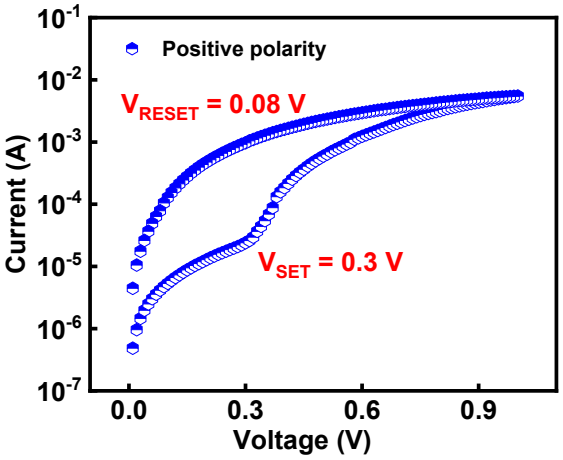

Figure S6: Semi-log graph of positive polarity which showing SET and RESET voltage.

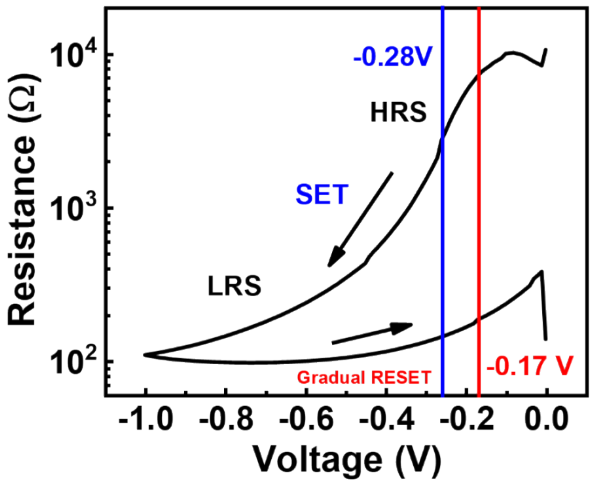

Figure S7: The resistance versus negative polarity voltage graph replotted in logarithmic scale.

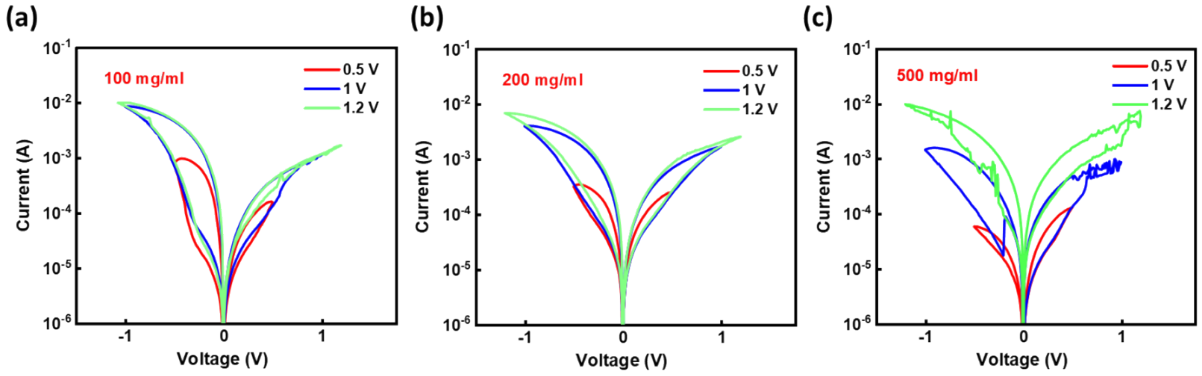

Figure S8: Voltage variation for all the three-solution concentrations (a) 100 mg/ml (b) 200 mg/ml and (c) 500 mg/ml.

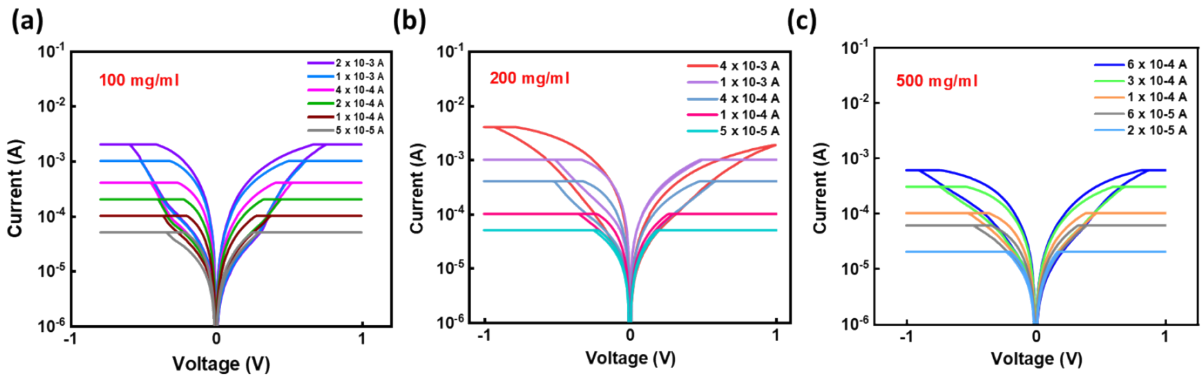

Figure S9: Variation of current compliance for all the three solution concentrations (a) 100 mg/ml (b) 200 mg/ml and (c) 500 mg/ml.

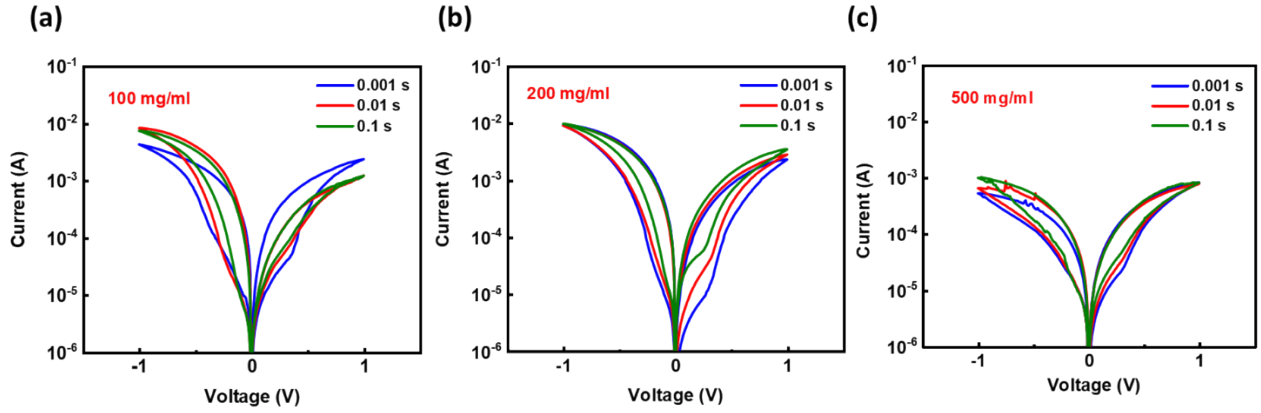

Figure S10: I-V characteristics for the three solution concentrations (a) 100 mg/ml (b) 200 mg/ml and (c) 500 mg/ml with varying time delay.

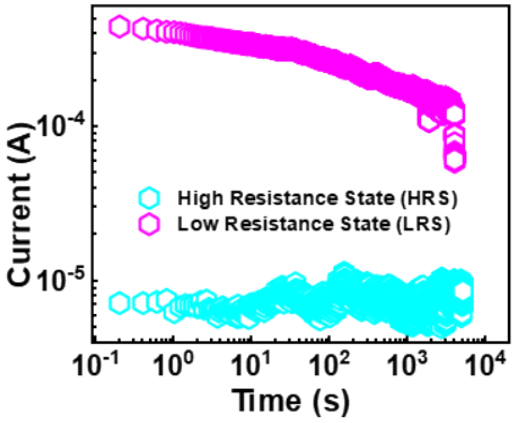

Figure S11: Retention characteristic of device recorded for $>10^3$ seconds to confirm device is volatile in nature.

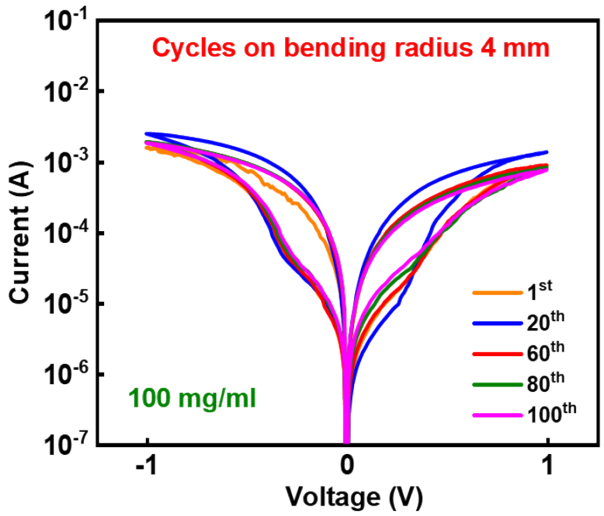

Figure S12: Multiple I-V cycles of 100 mg/ml solution concentration device bent at r = 4 mm,

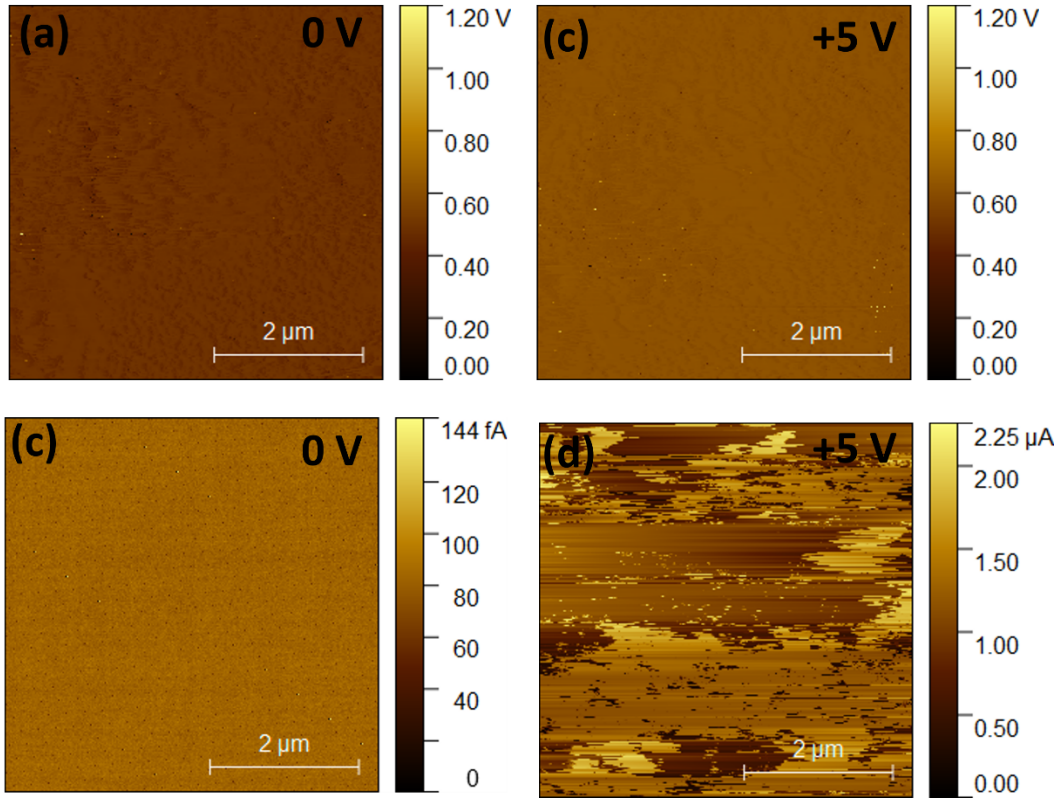

Figure S13: Surface potential image of (a) 0V, (b) +5 V of PbI_2 film on ITO/PET measured by Kelvin probe force microscopy (KPFM) across 5 × 5 um^2 scan area. (c) and (d) Current mapping biased at (c) 0V and (d) +5V, switching measured using conductive atomic force microscopy (c-AFM) 5 × 5 um^2 scan area.

Formation/rupture of the conducting channels due to redistribution of ions (halide and metal) within the active layer is an essential mechanism for the resistive switching phenomenon in PbI_2 based memristor devices. (*ACS Nano* **2016,** *10* (5), 5413-5418, *Adv. Mater.* **2016,** *28* (31), 6562-6567) However, it is difficult to discriminate these mechanisms in a device based solely on the *I-V* characteristics. Microscopic surface mapping of bare PbI_2 layer using a tip that does not diffuse into the PbI_2 layer can reveal or rule out the necessity of Ag filamentation and can highlight the role of space charge accumulation for the switching mechanism. Surface potential (SP) was measured by Scanning Kelvin probe microscopy (SKPM) across a 5 ×5 μm^2 scan area of PbI_2 film surface before voltage biasing **(Figure S13a)**. As seen, SP is uniformly distributed and rises abruptly across the all-scan areas under the external electric field by applying a positive bias of +5 V on the scanning probe (**Figure S13b**). After surface biasing SP increases ~400 mV, which suggests SET process can be triggered by an external electric field even without any top electrode. Note, PbI_2 film has many defects in the form of vacancies (V_{Pb}, V_I), interstitials (Pb_i, I_i), and anti-sites (Pb_I, I_{Pb}). (*Energy Environ. Sci.* **2015,** *8* (7), 2118-2127) Iodine vacancies (V_I) in PbI_2 film have lower activation energy between ~0.33 - 0.58 eV compared to Pb (2.31eV) and thus the diffusion barrier for easier migration. (*Adv. Mater.* **2017,** *29* (29), 1700527, *Nat. Comm.* **6**, 7497 (2015)) Therefore, the positively charged V_I are depleted and negatively charged iodine ions are readily accumulated at the film surface under the applied positive bias. Thus, this leads to the SP variation indicating the switching characteristics.

We have further conducted the current mapping of the top surface of PbI_2 film using the conductive mode (**Figure S13 c-d**). In this case, a positive bias of V = +5V was applied on the ITO as the bottom electrode while the conducting tip as the top electrode was grounded. The current mapping of the scan areas at 0V bias shows the order of femto-ampere (fA) from PbI_2 film and increased significantly to micro-ampere (μA) after applying a bias of V = +5V. As shown, the scanned area becomes conductive with a μA current, which shows the occurrence of the SET process. The significantly higher current level in the biased scanned area compared to the non-biased area, confirms that the SET process in PbI_2 films can be triggered without any top electrode, effectively confirming the role of iodine ions in switching mechanism.

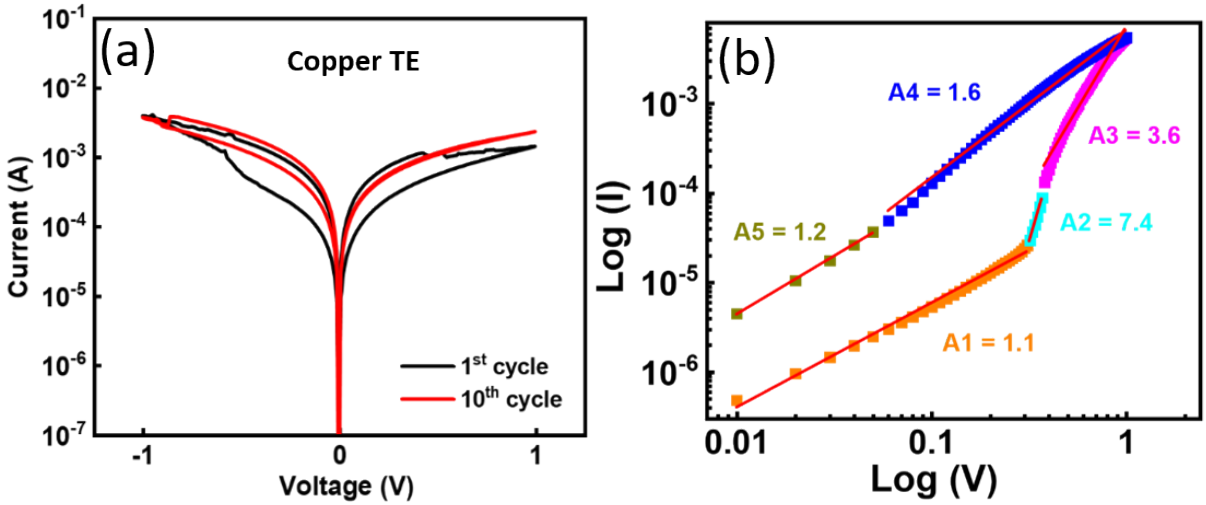

Figure S14: (a) I-V characteristics with copper as top electrode, (b) Log (I) – Log (V) graph showing fitted slope of conduction mechanism with Ag as top electrode. Devices were prepared using PbI_2 solution concentration as 100 mg/ml

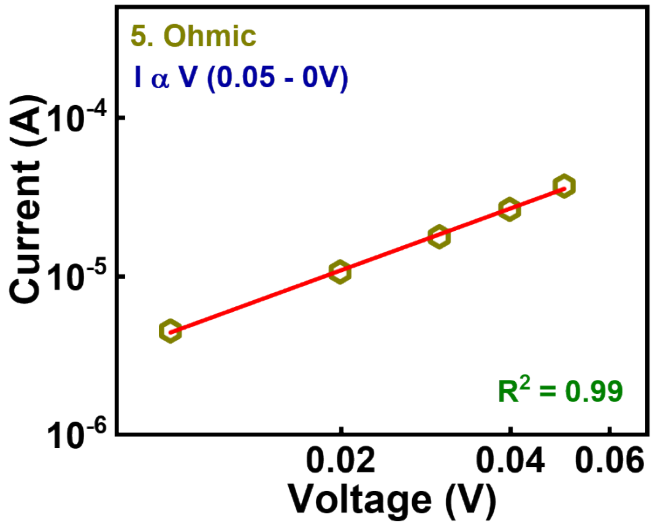

Figure S15: I α V graph of voltage range (0.08 – 1V) showing Ohmic conduction.

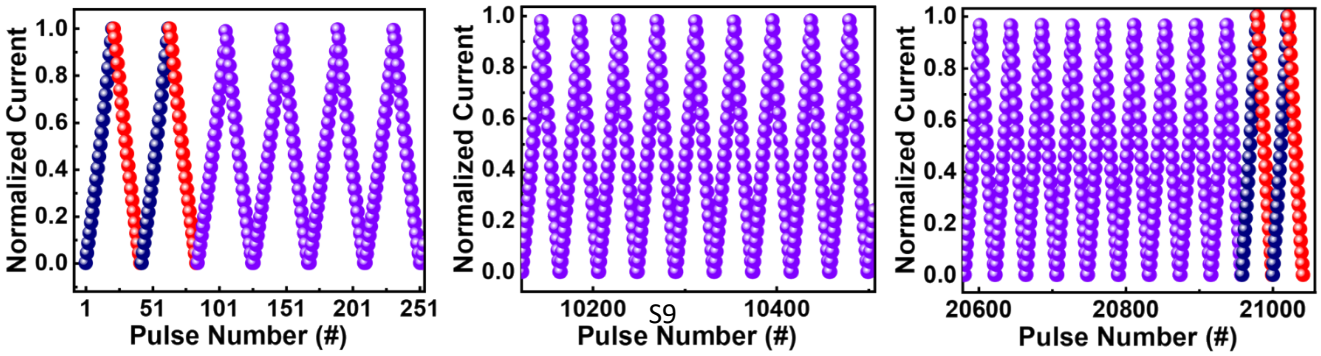

Figure S16: 20K Potentiation and Depression (P&D) cycles recorded on flat condition using Non-Identical Method.

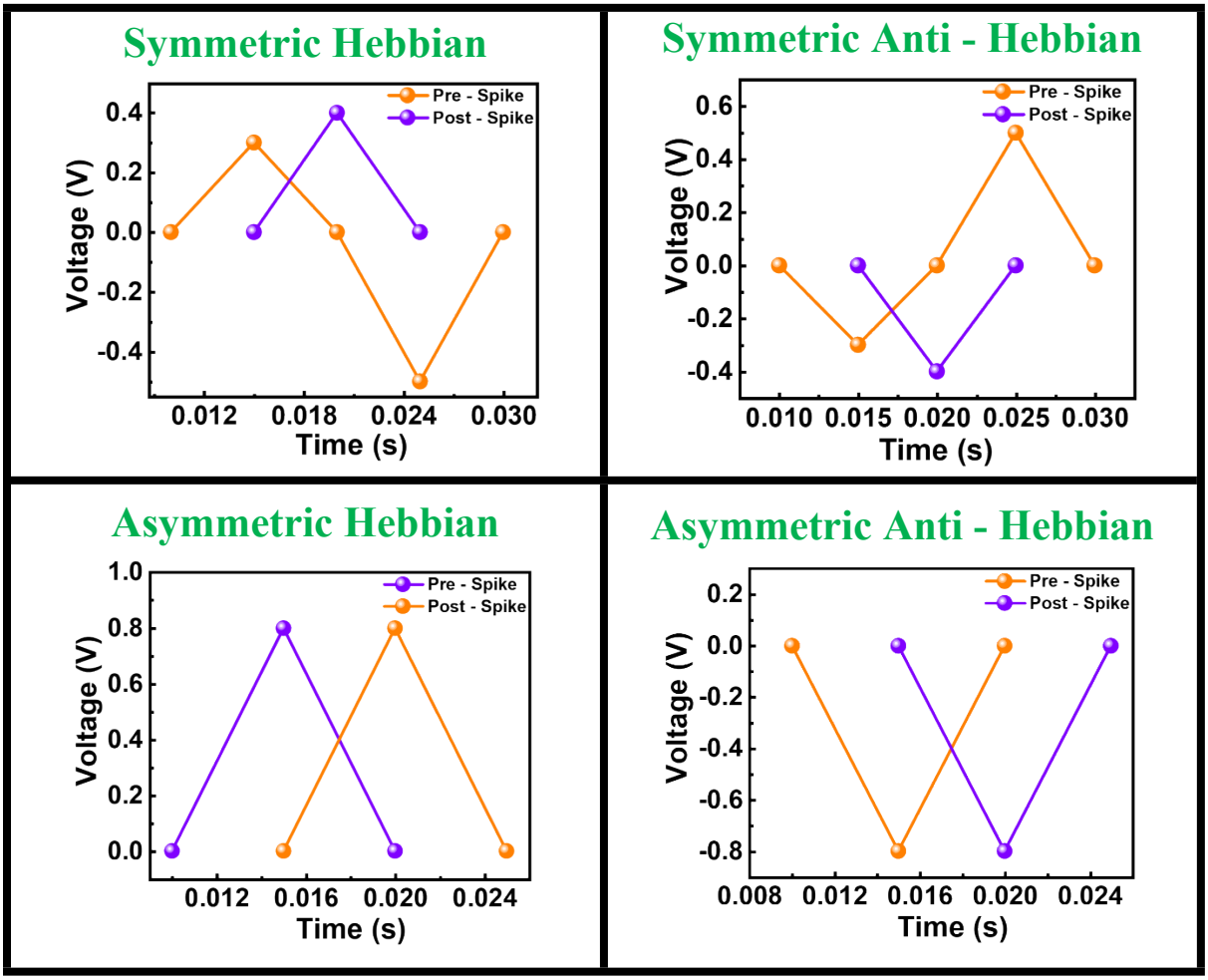

Figure S17: The pre and post synaptic pulses adopted to record all four STDP patterns.

Table S1: The comparison table of MNIST pattern recognition accuracy.

Sr. No.	Device Structure	No. of Epochs	Accuracy (%)	By simulation	Ref.
1	**PET/ITO/PEDOT:PSS/PbI_2/Ag (Bending condition : r = 4 mm)**	**30**	**95.06%**	**Yes**	**Our work**
2	$Al_2O_3/Ta_2O_5/Al_2O_3$	100	85%	Yes	[1]
3	Al/ZnO NPs/CuO NWs/Cu	1000	93%	Yes	[2]

4	P3HT base MemTs	500	92.53%	Yes	[3]
5	TiS3 - TiOx - TiS3	15	90%	Yes	[4]
6	2D MoS2 based memristor	200	84.70%	Yes	[5]
7	Pt/Ti3C2/Pt	40	80.60%	Yes	[6]
8	PCM device	500	82.00%	Yes	[7]

References

[1] J.P. Kim, S.K. Kim, S. Park, S.H. Kuk, T. Kim, B.H. Kim, S.H. Ahn, Y.H. Cho, Y.J. Jeong, S.Y. Choi, S. Kim, Dielectric-Engineered High-Speed, Low-Power, Highly Reliable Charge Trap Flash-Based Synaptic Device for Neuromorphic Computing beyond Inference, Nano Lett. 23 (2023) 451–461. https://doi.org/10.1021/acs.nanolett.2c03453.

[2] Y. Wang, W. Wang, C. Zhang, H. Kan, W. Yue, J. Pang, S. Gao, Y. Li, A Digital-Analog Integrated Memristor Based on a ZnO NPs/CuO NWs Heterostructure for Neuromorphic Computing, ACS Appl. Electron. Mater. 4 (2022) 3525–3534. https://doi.org/10.1021/acsaelm.2c00495.

[3] S. Sagar, K. Udaya Mohanan, S. Cho, L.A. Majewski, B.C. Das, Emulation of synaptic functions with low voltage organic memtransistor for hardware oriented neuromorphic computing, Sci. Rep. 12 (2022). https://doi.org/10.1038/s41598-022-07505-9.

[4] J.K. Qin, H.L. Sun, P.Y. Huang, Y. Li, L. Zhen, C.Y. Xu, Synaptic plasticity realized by selective oxidation of TiS3 nanosheet for neuromorphic devices, RSC Adv. 13 (2023) 14849–14854. https://doi.org/10.1039/d3ra00782k.

[5] C.H. Huang, H. Chang, T.Y. Yang, Y.C. Wang, Y.L. Chueh, K. Nomura, Artificial Synapse Based on a 2D-SnO2Memtransistor with Dynamically Tunable Analog Switching for Neuromorphic Computing, ACS Appl. Mater. Interfaces. 13 (2021) 52822–52832. https://doi.org/10.1021/acsami.1c18329.

[6] X. Zhang, H. Chen, S. Cheng, F. Guo, W. Jie, J. Hao, Tunable Resistive Switching in 2D MXene Ti3C2Nanosheets for Non-Volatile Memory and Neuromorphic Computing, ACS Appl. Mater. Interfaces. 14 (2022) 44614–44621. https://doi.org/10.1021/acsami.2c14006.

[7] D. Querlioz, O. Bichler, A.F. Vincent, C. Gamrat, Bioinspired Programming of Memory Devices for Implementing an Inference Engine, Proc. IEEE. 103 (2015) 1398–1416. https://doi.org/10.1109/JPROC.2015.2437616.